Global Biogeochemical Cycles

RESEARCH ARTICLE
10.1029/2020GB006623

Preformed Properties for Marine Organic Matter and Carbonate Mineral Cycling Quantification

B. R. Carter[1,2], R. A. Feely[2], S. K. Lauvset[3], A. Olsen[4], T. DeVries[5], and R. Sonnerup[1]

[1]Cooperative Institute for the Climate, Ocean, and Ecosystem Studies, formerly Joint Institute for the Study of the Atmosphere and Ocean, University of Washington, Seattle, WA, USA, [2]Pacific Marine Environmental Laboratory, National Oceanic and Atmospheric Administration, Seattle, WA, USA, [3]NORCE Norwegian Research Centre, Bjerknes Centre for Climate Research, Bergen, Norway, [4]Geophysical Institute, Bjerknes Centre for Climate Research, University of Bergen, Bergen, Norway, [5]Department of Geography and Earth Research Institute, University of California, Santa Barbara, CA, USA

Key Points:
- We have updated global preformed biogeochemical property estimates and provided the estimates for analysis and model validation
- The updated estimates support recent literature findings regarding remineralization ratios and deficiencies in apparent oxygen utilization
- Carbonate mineral dissolution rates are likely more uniform between saturation regimes than previously found

Supporting Information:
- Supporting Information S1

Correspondence to:
B. R. Carter,
brendan.carter@noaa.gov

Citation:
Carter, B. R., Feely, R. A., Lauvset, S. K., Olsen, A., DeVries, T., & Sonnerup, R. (2021). Preformed properties for marine organic matter and carbonate mineral cycling quantification. *Global Biogeochemical Cycles*, *35*, e2020GB006623. https://doi.org/10.1029/2020GB006623

Received 8 APR 2020
Accepted 2 DEC 2020
Accepted article online 11 DEC 2020

Abstract We estimate preformed ocean phosphate, nitrate, oxygen, silicate, and alkalinity by combining a reconstruction of ventilation pathways in the ocean interior with estimates of submixed layer properties. These new preformed property estimates are intended to aid biogeochemical cycling studies and validation of modeled preformed property distributions and are available online. Analyses of net property accumulations (observed minus preformed properties) indicate net remineralization ratios in the ocean interior of [1 P]: [14.1 ± 0.6 N]: [−141 ± 12 O_2]: [95 ± 25 Si]: [89 ± 9 TA]. These ratios imply that the interior ocean stores 1,300 (±230) PgC through organic matter remineralization and 540 (±60) PgC through carbonate mineral dissolution and that apparent oxygen utilization can overestimate the interior ocean oxygen consumption by ~25%. Further, only 4 (±1%) and 46 (±5%) of the total alkalinity accumulated from carbonate mineral dissolution are found in seawater that is supersaturated with respect to the aragonite and calcite mineral forms of calcium carbonate, respectively. These small excess alkalinity inventories are due to smaller volumes of the supersaturated water masses and shorter ventilation timescales, as carbonate mineral dissolution rates appear nearly independent of depth and saturation state.

1. Introduction

Preformed ocean properties are those that seawater had when last in the surface mixed layer and are useful for quantifying biogeochemical cycling and mixing processes in the ocean interior. Preformed properties allow the impacts of interior ocean processes to be distinguished from the effects of surface ocean exchanges of heat, gases, nutrients, and freshwater (e.g., Feely et al., 2002; Feely, Sabine, Lee, et al., 2004; Pardo et al., 2011; Sabine et al., 2002, 2004; Sabine & Tanhua, 2010). Variations in preformed nutrient inventories are strongly linked with the strength of ocean carbon sequestration (Marinov et al., 2008) and allow estimation of the initial properties that govern the amount of a dissolved gas or its byproducts present at air-sea equilibrium. This is critical information for estimating the quantity of additional dissolved inorganic carbon (C) present in seawater due to anthropogenic CO_2 emissions (e.g., Sabine et al., 2002, 2004).

A definition of "surface mixed layer" is required when defining preformed properties; however, there is no depth range over which the ocean is perfectly mixed nor is there an exact depth below which there is no exchange with near-surface waters. It can therefore be asked, "at what point can water properties be called preformed?" Apparent oxygen utilization ($AOU = O_{2at\ atmospheric\ equilibrium} - O_{2measured}$), for example, implicitly assumes that water is preformed when it is fully equilibrated with respect to atmospheric oxygen. AOU is complicated by the fact that air-sea disequilibria are common within deep winter mixed layers where surface exchanges are still important (Carter, Talley, et al., 2014; Talley et al., 2003), and O_2 is often undersaturated in waters detrained from mixed layers (i.e., left behind after seasonal mixed layer shoaling). Carter, Talley, et al. (2014) define preformed properties as the properties of interior water masses at the moment they leave surface mixed layers for the final time before being advected from the formation region. In this study, we adopt this definition and note that preformed properties can be significantly out of equilibrium with respect to the atmosphere, particularly in the Southern Ocean and other deep water formation regions (e.g., Russell & Dickson, 2003).

Remineralization ratios—or how chemical species are affected by organic matter remineralization relative to one another—can be estimated from preformed properties and interior ocean property distributions. Remineralization ratios are widely used in oceanography to estimate the fractions of property distributions that can be attributed to the cycling of organic carbon, thereby allowing the impacts of other processes to be estimated by residual (e.g., Feely et al., 2002, 2016; Feely, Sabine, Lee, et al., 2004; Gebbie et al., 2010; Russell & Dickson, 2003; Sabine et al., 2002). Many remineralization ratio estimates exist in the literature (e.g., Anderson & Sarmiento, 1994; Hedges et al., 2002; Li & Peng, 2002; Redfield, 1934; Redfield et al., 1963; Takahashi et al., 1985). Redfield et al.'s (1963) ratio of phosphate (P): nitrate (N): C:-O_2 of 1:16:106:138 was one of the first estimates and was based on elemental ratios in organic matter and evident in seawater. Later analyses of property changes along isopycnals suggested the P:-O_2 ratio needed to be revised upward nearer to ~170 (Anderson & Sarmiento, 1994; Takahashi et al., 1985). The most recent analyses have emphasized that neglecting diapycnal diffusivity could have biased these estimates higher (as also explored by Anderson & Sarmiento, 1994) and suggested that the lower P:-O_2 ratios could be more accurate (Carter, Talley, et al., 2014; Li & Peng, 2002). DeVries and Deutsch (2014)'s analysis of regeneration ratios shows -O_2:P of 147 $\pm$ 6, which agrees with the 150:1 ratios based on the average biochemical composition of phytoplankton (Anderson, 1995; Emerson & Hedges, 2008). Recently, analysis of nutrient distributions using ocean circulation models suggests that P:N:C:-O_2 regeneration ratios vary as much as threefold to fourfold across oceanographic biomes (Deutsch & Weber, 2012; DeVries & Deutsch, 2014; Teng et al., 2014; Weber & Deutsch, 2010). The regional nutrient regeneration patterns determined in these studies are consistent with direct analyses of the elemental composition of aggregates of particulate organic matter (Martiny et al., 2013), with low N:P ratios being found in subpolar regions and high N:P ratios in subtropical regions.

Preformed properties have also been used to quantify the net impacts of precipitation and dissolution of carbonate minerals. Milliman and Droxler (1996) and Milliman et al. (1999) argued that as much as 60% to 80% of carbonate mineral export is dissolved in the upper 500–1,000 m. Feely et al. (2002) and Berelson et al. (2007) evaluated alkalinity concentrations in excess of preformed in the Pacific (i.e., excess total alkalinity, or TA) and ultimately supported this conclusion. $CaCO_3$ dissolution occurring in $CaCO_3$-supersaturated seawater implies that biological mediation of the dissolution process must be important (Milliman et al., 1999). However, Friis et al. (2006, 2007) later showed that interior ocean mixing can account for the observed distributions of carbonate mineral dissolution byproducts even in the absence of dissolution in supersaturated waters, so the fraction of dissolution occurring in supersaturated environments remains under debate.

Preformed properties have been estimated in a variety of ways. Feely, Sabine, Lee, et al. (2004) used regressions relating TA to conservative and quasi-conservative surface seawater properties (specifically potential temperature θ, salinity S, and a combination of phosphate and oxygen, PO; Broecker, 1974) from each ocean basin to estimate the interior ocean preformed properties in the same basins. This approach has the limitation that surface ocean measurements are typically biased toward summer, especially at high latitudes, limiting their applicability because ocean interior waters are usually subducted in late winter (Stommel, 1979). In addition, some deep water masses are ventilated in basins other than where they are found (e.g., Talley, 2013). Pardo et al. (2011) used properties from 75–180 m depth as preformed values, but interior mixing and circulation limit application of these estimates to interior ocean waters that are very near their ventilation regions. Preformed TA estimations benefit from strong relationships between TA and other seawater properties, like salinity (S), that allow accurate regression-based estimates. Regression-based approaches are more difficult for oxygen and macronutrients as they are more strongly affected by biological cycling and gas exchange. Regressions have therefore not been used to estimate preformed macronutrient and oxygen concentrations, prior to this study.

Here we combine updated versions of recent regression methods (Carter et al., 2017) with interior ocean mixing pathways (Devries, 2014; Gebbie et al., 2010; Khatiwala, 2007), a mixed layer depth climatology (Holte et al., 2017), and a gridded interior ocean biogeochemical data product (Lauvset et al., 2016) to produce full-ocean preformed property estimates that avoid some of the issues with the previous approaches. We then use these distributions to infer net apparent remineralization ratios, regional net denitrification, net oxygen consumption, and net calcium carbonate cycling in interior ocean water masses. The primary goal of

this effort is to present and quantify the preformed properties and discuss their potential applications, as there is more analysis to be done for each of the biogeochemical applications briefly discussed here.

2. Methods

Our approach for estimating preformed properties and their uncertainty combines several methods in several steps. First, we trace interior ocean water mass mixtures back to where they were last ventilated using flow fields from several different ocean circulation models. Next, we estimate properties at the base of the deepest seasonal mixed layers in these locations, and weight the property estimates by the relative contributions of each surface location to the interior water mass mixtures, thus determining the preformed property estimates at each interior location. The property estimates made at the base of the mixed layers are thought to be the best estimates of the properties of the seawater that is detrained into the ocean interior through the shoaling of the seasonal mixed layer (Stommel, 1979). A variant on this approach was used by Lauvset et al. (2020) to estimate preformed alkalinity. We estimate uncertainty by varying aspects of our procedure and evaluating the effects on the resulting estimates (Supporting Information S1).

2.1. Ventilation Pathways

To infer where interior ocean water masses were last near the ocean surface, we use ocean ventilation pathways captured by the transport matrix output from a data-assimilating ocean circulation inverse model (OCIM: Devries, 2014). Observations of potential temperature, salinity, radiocarbon, and CFC-11—in addition to reanalysis products for surface heat and freshwater fluxes and mean dynamic topography—are assimilated to estimate the climatological mean state of the ocean circulation (Devries, 2014; DeVries & Primeau, 2011). As a measure of uncertainty resulting from transport estimates, we also use two other transport matrix products, a transport matrix version of a 3-D circulation model (Khatiwala, 2007), and the mixing pathways produced by the Total Matrix Intercomparison (TMI) approach of Gebbie et al. (2010) (Supporting Information S1). We rely foremost on the OCIM product because it has global coverage, the highest spatial resolution; is optimized through data assimilation; and does not rely on remineralization ratios to infer circulation pathways. For our base case, we use the CTL version of OCIM1, which was also used to estimate ocean anthropogenic CO_2 uptake (Devries, 2014). The resolution of the model is ~2° × 2° in the horizontal, with 24 vertical levels ranging in thickness from 36 m at the surface to ~600 m in the deep ocean.

We use these transport matrices to determine where mixtures of waters that comprise interior ocean water parcels were last at the ocean surface, producing an array $F_{i,k}$ that quantifies the fraction of water from each of the k surface grid cells present in each of the i interior ocean grid cells (see Supporting Information S2 for details). For the OCIM, $k = 10{,}441$, and $i = 189{,}717$. For example, water at 1,300 m depth in the North Pacific may have a partial source in the surface North Pacific, the Southern Ocean, and the North Atlantic Ocean (Figure 1).

2.2. Property Estimates for Ventilation Regions

We adopt two approaches for estimating the properties that detrain from deep seasonal mixed layers during the springtime mixed layer shoaling: a regression-based approach and an interpolation-based approach. Preformed property distributions from both approaches are provided at the GitHub link, and differences between the two estimates are included in the uncertainty assessment (Supporting Information S1). However, only results from the regression-based approach are presented in the figures and tables in the main manuscript.

The first approach uses locally interpolated regressions (LIRs; Carter et al., 2017) to estimate the preformed properties of the seawater that leaves each surface grid cell, basing the estimate on the temperature and salinity values of the interior ocean mixtures. The LIR MATLAB routines generate estimates of seawater properties using regressions that are specific to user-input ocean latitude, longitude, and depth coordinates; the routines interpolate collections of prefit coefficients (α) to these user-input coordinates. The α coefficients are prefit by Carter et al. (2016, 2017) to data from GLODAPv2 (Olsen et al., 2016) gathered within latitude, longitude, and depth/density windows around all points on a 3-D ocean grid. For the current application, the user-provided coordinates are the latitudes, longitudes, and the deepest monthly-mean mixed layer depths of the surface grid cells, as interpolated from Holte et al. (2017)'s mixed layer depth

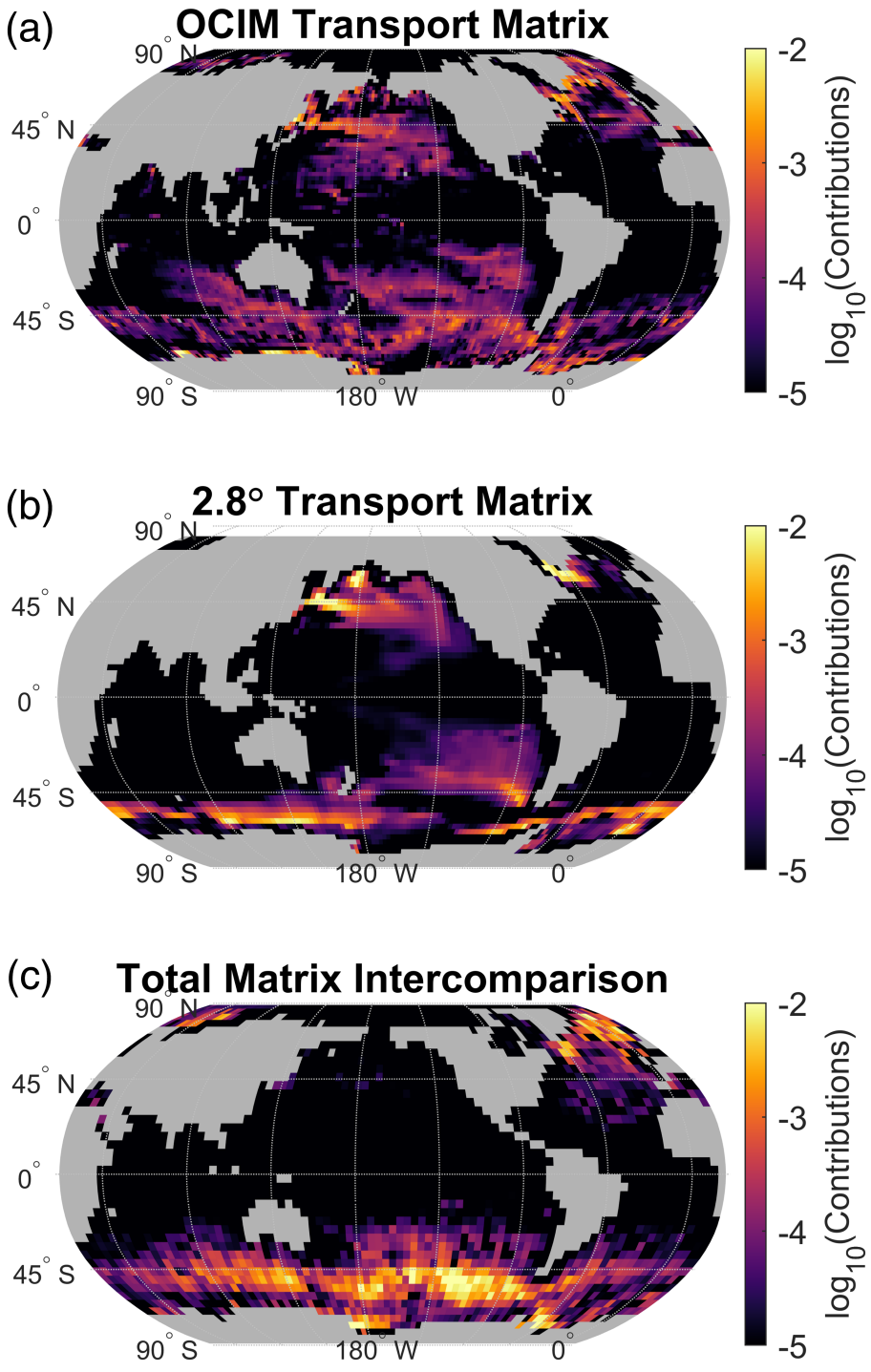

Figure 1. Maps showing example mixing fractions or $\log_{10}$ of fractional mass contributions from surface grid cells to the interior ocean grid cells nearest 160°W, 30°N, and ~1,300 m depth. Maps are provided for the primary circulation product used for this analysis, (a) the 2° × 2° CTL OCIM1 data-assimilated model transport matrix reduction of Devries (2014), as well as for the two products used to test the sensitivity of the results to the assumed physical circulation; (b) the 2.8° transport matrix from Khatiwala (2007); and the (c) 4° × 4° total matrix intercomparison product of Gebbie et al. (2010). Water at the base of the Northern Pacific Subtropical Gyre thermocline is chosen for these examples to highlight the convergence of water types in this region and emphasize the differences in the circulation pathways that can be simulated by the various approaches used.

climatology or 100 m, whichever is deeper. This minimum depth threshold is used to ensure the LIRs use coefficients that are fit to data that span more than the seasonally biased surface layer. The sensitivity of the results to this minimum depth threshold for the LIR is tested and included in the uncertainty assessment (Supporting Information S1. The predictors in the regressions are the interior ocean θ and S (i.e., Regression 8 in Supporting Information S3):

$$X_{i,k} = \alpha_{0,k} + \alpha_{S,k} S_i + \alpha_{\theta,k} \theta_i. \quad (1)$$

Here $X_{i,k}$ is the seawater property at the kth base-of-the-mixed-layer location estimated using the observed S and θ of the ith interior-ocean grid cell. This approach provides a best-estimate answer to the question, "what would the biogeochemical properties of a water type be if it had detrained from this (kth) surface ocean location and had the same salinity and temperature as this other (ith) interior ocean mixture?"

The regressions are specific to each combination of surface coordinates (10,441 regressions for each latitude, longitude, and mixed layer depth combination) and are used to estimate preformed properties for each combination of interior ocean salinities and temperatures (189,717 interior ocean S and θ combinations). Measures taken for computational efficiency (described in Supporting Information S3) reduce the computational burden from ~2 billion to ~29 million such computations.

One problem with this regression approach, as well as for all previous regression approaches for estimating preformed properties, is that interior ocean physical properties (i.e., S_i, and θ_i) can be the result of mixing between many different parcels of water, each with initial physical properties that are different from those in the final mixture. The distant interior-ocean physical seawater properties used for LIR-based estimates of $X_{i,k}$ at the base of the mixed layers may not be realistic predictors for the surface outcrop locations. We therefore use the differences between the interior ocean physical properties (i.e., the θ_i and S_i where we are estimating the preformed property mixture) and the "base of the mixed layer" physical properties (i.e., the θ_k and S_k where the subducting seawater components originate) interpolated from the GLODAPv2 gridded product (Lauvset et al., 2016) as an estimate of uncertainty in our predictors. We use this information as input uncertainties in the LIR routines (Carter et al., 2016) to estimate an uncertainty for the output $X_{i,k}$ (i.e., $U_{i,k}$) that scales with the differences in the physical properties between the interior and sub-mixed layer cells. This uncertainty is used as a weighting term in determining preformed property estimates (section 2.3).

The second approach for determining base-of-the-mixed-layer properties is a direct linear interpolation of the GLODAPv2 gridded product to the depth of the deepest monthly-mean mixed layer depths. The direct interpolation approach is simpler than the regression-based approach, but it is also more sensitive to the assumed mixed layer depth threshold and, especially, to the assumed circulation patterns (Supporting Information S1). This is because ocean properties tend to vary strongly with respect to depth near the base of the mixed layer, so slight mismatches between modeled and actual ocean circulations, or between the mixed layer depths in the mixed layer climatology and the GLODAPv2 gridded product, lead to biases in preformed properties estimated in this way. By contrast, the regression-based approach relies upon emergent empirical relationships between properties in the vicinity of each location, so these mismatches are less important. A second reason to prefer the regression-based approach is that one might imagine that multiple water types can emerge from a single surface grid cell depending on the time of year of mixed layer detrainment or the intensity of convection each year, and the regression approach allows these variable water types to emerge from a single surface grid cell by varying interior-ocean θ_i and S_i used as a regression predictor. The interpolation-based estimates serve as a useful comparison, however, and it results in preformed properties that, when averaged between calculations with different depth thresholds and circulation assumptions, are qualitatively and quantitatively similar to the regression-based estimates.

2.3. Preformed Property Estimates

For each ith interior ocean grid cell, the $F_{i,k}$ mixing fraction estimates are multiplied by the regression-based $X_{i,k}$ seawater property estimates and a weighting term ($W_{i,k}$, equaling ${U_{i,k}}^{-2}$), and a weighted average is calculated to yield the ith preformed property estimate (X^0):

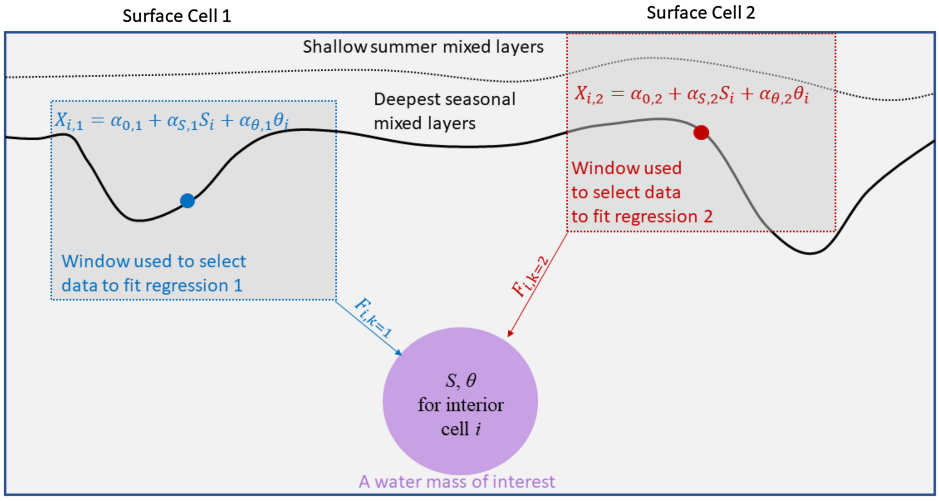

Figure 2. A schematic showing how the regressions are centered (red and blue dots) on the base of the deep winter mixed layers but are fit using data from within and below the mixed layers (red and blue-outlined gray boxes) and how preformed estimates from various, often distant, locations are combined using mixing fractions (F values) to form the combined preformed estimate of the purple ith interior ocean mixture. Only two contributing surface sources are shown in this schematic, but, in the OCIM-based estimates, there are 10,441 F values (many equaling 0) for each interior ocean location that relate the interior mixtures to the 10,441 surface grid cell sources. The mixing fractions are combined using Equations 2 and 3.

$$X_i^0 = \frac{\sum_{k=1}^{10,441} F_{i,k} X_{i,k} W_{i,k}}{\sum_{k=1}^{10,441} F_{i,k} W_{i,k}}. \quad (2)$$

A schematic shows the elements of this calculation for a simplified case in which an interior ocean grid cell only has two surface contributions (Figure 2).

The equivalent equation for the interpolation-based approach is simpler because it has neither the weighting term nor property estimates that vary with the interior ocean predictor distributions:

$$X_i^0 = \sum_{k=1}^{10,441} F_{i,k} X_k. \quad (3)$$

These equations are used to produce preformed values P^0, N^0, $O_2{}^0$, Si^0, and TA^0 for each of the 189,717 subsurface grid cells. We compute "potential alkalinity" (pTA, and similarly for the related preformed potential alkalinity pTA^0) as TA + 1.36*N to account for the small impacts of organic matter cycling on TA distributions (Wolf-Gladrow et al., 2007). These estimates are on the transport matrix grid, so a three-dimensional Delaunay triangulation (i.e., linear interpolation) is used to shift them onto the grid used for the gridded GLODAPv2 data product (Lauvset et al., 2016; Olsen et al., 2016). In most locations, this does not add significant errors (possible exceptions include the Artic and Mediterranean when using Khatiwala, 2007, matrix, which does not cover these basins/seas). X^0 for depths that are shallower than the deepest monthly-mean mixed layer depths is not meaningful and is not included in this analysis, nor are values in marginal seas since both the LIR regressions and the water mass ventilation pathways are less well constrained in these regions. This combined grid mask is also provided within the preformed property data files. All preformed property estimates and their uncertainties are provided on the GLODAPv2 grid used by Lauvset et al. (2016), which is identical to the World Ocean Atlas 2009 grid, in the NetCDF and Hierarchical Data Format (HD5, used by MATLAB) formats.

2.4. Ideal Ages and Property Accumulation Rates and Ratios

Preformed properties are sometimes used to infer accumulation or utilization rates from calculations that also require water mass age information (e.g., Berelson et al., 2007; Feely, Sabine, Schlitzer, et al., 2004; Sonnerup et al., 2015). Rate estimates are not a primary intended product for this effort, and we caution that there can be significant difficulties with interpreting calculations that directly combine accumulations with

age information. We nevertheless calculate some accumulation rates to inform our discussion and allow comparisons with other studies that used preformed properties and AOU with age information to calculate rates.

Ideal ages are calculated using methods described in DeVries and Primeau (2011) with the boundary condition equalling the surface mixed layers as defined earlier, including the minimum-depth threshold of 100 m. The mass-weighted average ideal age calculated with this inclusive boundary condition is 580 ($\pm$5, 1σ) yr, which is only slightly shorter than the 593 yr average age obtained when only using surface grid cells as a boundary. The uncertainties on these ideal ages are likely underestimated because they do not include contributions from variability between circulation estimates (they only represent uncertainty from the minimum mixed layer depth cutoff). It should also be noted that additional uncertainties are incurred when combining modeled circulation fields with observed mixed layer depth distributions, as is done for our rate estimates.

For comparison with literature, we use a regression method adapted from Berelson et al. (2007) and detailed in Supporting Information S4 to produce carbonate dissolution rate estimates. It is unclear the degree to which this regression approach is effective at eliminating the effects of dissolution that occurs outside of the regions of interest (see, e.g., Friis et al., 2006, 2007) or in dealing with biases resulting from mixing operating on the differing gradients of ideal age versus accumulations of TA (see, e.g., Koeve & Kähler, 2016). There may therefore be unresolved biases in these estimates. We do not present accumulation rates for organic matter remineralization because these estimates have large uncertainties due in part to uncertain cutoffs chosen for minimum mixed layer depths and water mass ages (see Supporting Information S4).

3. Results and Discussion

3.1. Preformed Property Distributions

The deepest waters (Figure 3, right column) reflect a balance between two main water types: North Atlantic Deep Water (NADW) and Antarctic Bottom Water (AABW) (Talley, 2013). NADW is low in preformed nutrients and rich in preformed dissolved oxygen because of the biological production and air-sea gas exchange that takes place as its source waters travel north at the surface in the Atlantic, while the AABW is rich in preformed nutrients (Figures 3d, 3h, and 3p, at 4,000 m south of 60°S) but low in preformed oxygen (Figure 3l) because the source waters (upwelled nutrient-rich Circumpolar Deep Water, CDW) spend much less time at the surface and are partially shielded from gas exchange by sea-ice before sinking back into the deep. AABW also has higher preformed potential alkalinity than NADW from carbonate mineral dissolution (Figure 3t), but the elevated preformed potential alkalinity of AABW is muted relative to nutrients because NADW is saltier than AABW and freshwater removal increases both salinity and alkalinity. These observations apply broadly from 2,500 to 4,000 m depth, though the domain dominated by AABW extends farther north into the Atlantic with greater depth (Figure 3).

The influence of intermediate and mode waters is visible in the subtropics along the 1,000 m depth surface (Figures 3b, 3f, 3j, 3n, and 3r), particularly in the Southern Hemisphere where Antarctic Intermediate Water (AAIW) ventilates the bases of the gyre thermoclines. AAIW formation involves injections of well-ventilated nutrient-rich surface waters into CDW that is oxygen poor and nutrient rich (Carter, Talley, et al., 2014; Naveira Garabato et al., 2009). AAIW is therefore initially undersaturated with respect to oxygen (Russell & Dickson, 2003) yet appears as a slight maximum in preformed oxygen (Figure 3j) in a band of high preformed nutrients (Figures 3b and 3f) in the southern Indian and Pacific Oceans between 20°S and 40°S. Forming as mixtures between moderately high-nutrient surface waters and high-nutrient deep waters, AAIW has slightly less preformed nutrients than AABW, but significantly more than NADW (Figures 3b and 3f; North Atlantic). Intermediate waters have lower preformed silicate than might be expected from phosphate and nitrate. This is because silicate is stripped from surface waters more rapidly and at more poleward latitudes (Sarmiento et al., 2004) and is remineralized deeper than phosphate (e.g., Holzer et al., 2014). Both processes reduce the quantity of silicate that is returned to the surface with Upper CDW (UCDW) and becomes incorporated into mode and intermediate water. A significant portion of the mid-depth North Atlantic has low preformed oxygen and elevated pTA^0 where warm, salty, alkaline, and low-O_2 Mediterranean Sea Intermediate Water is found (Figures 3j and 3r; between 20°N and 45°N).

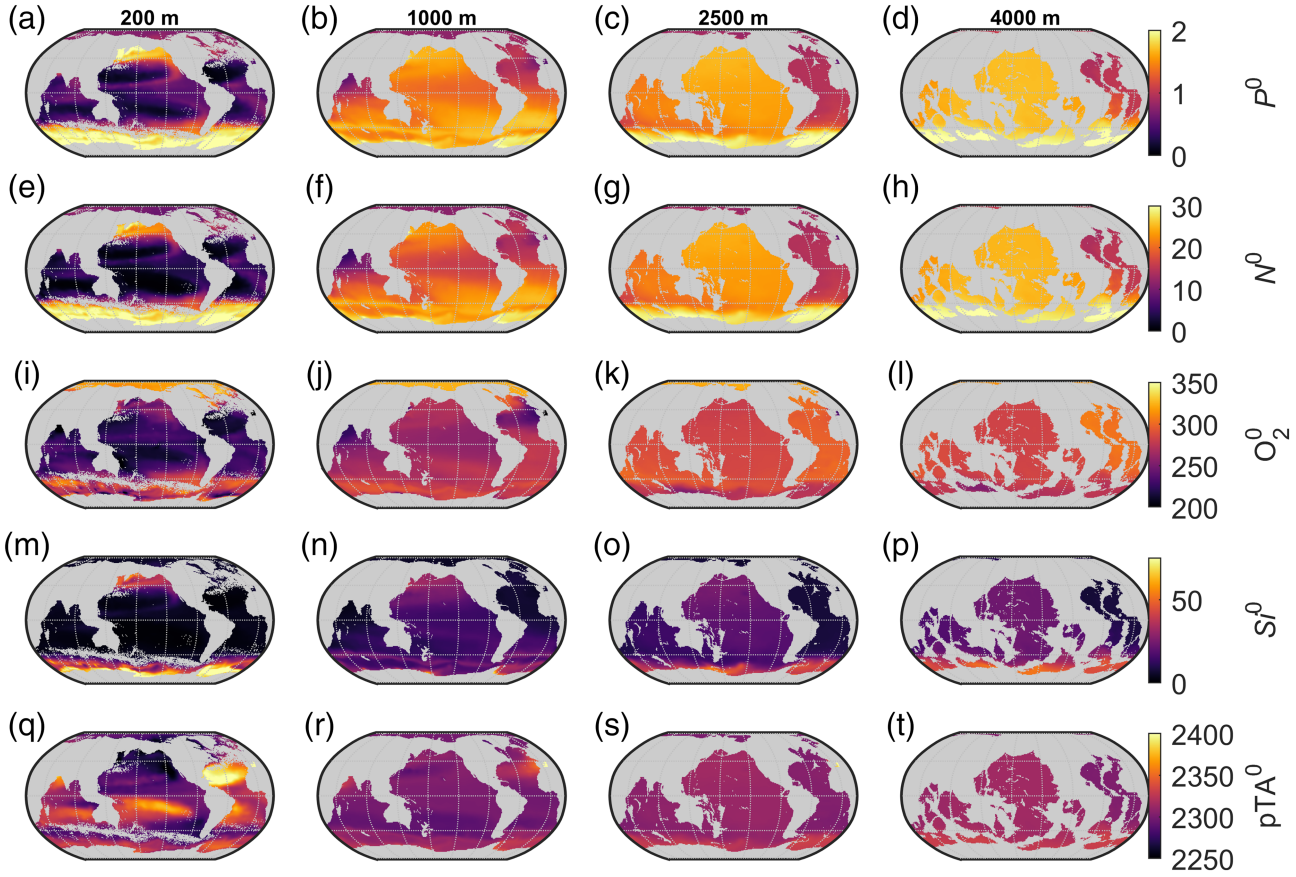

Figure 3. Global maps split at 20°E of preformed property concentrations estimated along the (first column) 200 m, (second column) 1,000 m, (third column) 2,500 m, and (fourth column) 4,000 m depth surfaces for (top row) phosphate, (second row) total nitrate and nitrite, (third row) dissolved oxygen molecule or O_2, (fourth row) silicate, and (bottom row) potential total alkalinity. Gyre structures are most visible near the surface, whereas basin-to-basin differences are more pronounced at depth. Gray areas are either land or regions where the deepest mixed layers are deeper than the depth surface. All units are μmol kg^{-1}.

The influence of many major water types can be seen in shallow subsurface waters (i.e., at 200 m). Subtropical gyre waters are generally low in nutrients (Figures 3a, 3e, and 3m; between 45°N and 45°S), associated with subduction of nutrient-depleted subtropical mode waters. Higher preformed nutrient concentrations occur below regions of surface divergence (i.e., upwelling): in the subpolar gyres (south of 45°S and north of 45°N), the Southern Ocean (south of 60°S), the equatorial regions (±10°N), and along eastern boundaries of ocean basins where mode, intermediate, and deep waters return to the surface. Preformed subsurface oxygen looks like the opposite of subsurface temperature due to the temperature dependence of O_2 solubility. Preformed oxygen is low in the oxygen deficient zones of the Eastern Tropical Pacific and the Arabian Sea relative to concentrations in high-latitude surface waters, suggesting that low initial oxygen due to warm temperatures contributes to the formation of the oxygen deficient zones.

3.2. Property Accumulations

The property accumulations are consistent with principles that have been long understood in oceanography (Table 1; Figure 4; Figure S1 has zonal integral sections by basins). The deep ocean progresses in age from the young North Atlantic to the old North Pacific, with accumulation of nitrate, phosphate, silicate, and potential alkalinity, and reduction of O_2 along this path. There is a strong maximum in remineralized phosphate and nitrate and utilized O_2 near 1,000 m depth—particularly in the North Pacific—and in the shallow subsurface (i.e., at 200 m) in the oxygen deficient zones near the equatorial upwelling zones (Figures 4a, 4e, and 4i; within ±20°N of the equator, and wider on the eastern edges). These maxima occur shallower than the oldest (i.e., least-recently ventilated) waters because sinking organic matter remineralization rates are higher shallower in the water column (e.g., Martin et al., 1987). This subsurface maximum is deeper for potential alkalinity than for N (Figures 4f and 4g vs. 4r and 4s) because the deep ocean is more

Table 1
Net Property Accumulations by Ocean Regions

	P	N	O_2	*Si*	pTA
Global	1.02 (±0.18)	14.4 (±2.8)	−143 (±15)	96 (±20)	90.0 (±9.4)
Atlantic and Arctic (north of 40°S)	0.12 (±0.02)	1.8 (±0.3)	−15 (±1)	6 (±2)	8.0 (±0.5)
Pacific (40°S to 67°N)	0.59 (±0.1)	8.3 (±1.5)	−85 (±8)	56 (±10)	55.0 (±5.6)
Indian (north of 40°S)	0.17 (±0.03)	2.4 (±0.5)	−22 (±2)	15 (±3)	15.0 (±1.5)
Southern (south of 40°S)	0.14 (±0.04)	1.9 (±0.6)	−21 (±4)	19 (±6)	12.0 (±2.5)

Note. Uncertainties are estimated at ±1σ. Units are Pmol.

chemically corrosive for carbonate minerals than is the shallow ocean (Carter, Toggweiler, et al., 2014; Ingle, 1975; Jiang et al., 2015) and, potentially, because carbonate minerals sink more efficiently or are remineralized/dissolved less efficiently than organic matter (Francois et al., 2002; Klaas & Archer, 2002). Silicate has an even deeper maximum accumulation (Figure 4p). This reflects its deeper remineralization profile than organic matter (e.g., Holzer et al., 2014) and the consumption of silicate by diatoms at high latitudes (Dunne et al., 2007; Henson et al., 2012; Honjo et al., 2008), which removes the majority of the surface ocean silicate near where it upwells in the polar and subpolar latitudes, before it can become entrained into the mode and intermediate waters that dominate the subtropical subsurface and intermediate ocean depths. Upwelling from these water masses supplies nutrients to the subtropical surface ocean (Sarmiento et al., 2004), and the low concentrations of upwelling *Si* leads to a low subtropical surface export of *Si* to the subtropical gyre thermocline water masses, and thus low Δ*Si*. Total nutrient and potential alkalinity accumulations and net oxygen consumptions increase from the Atlantic

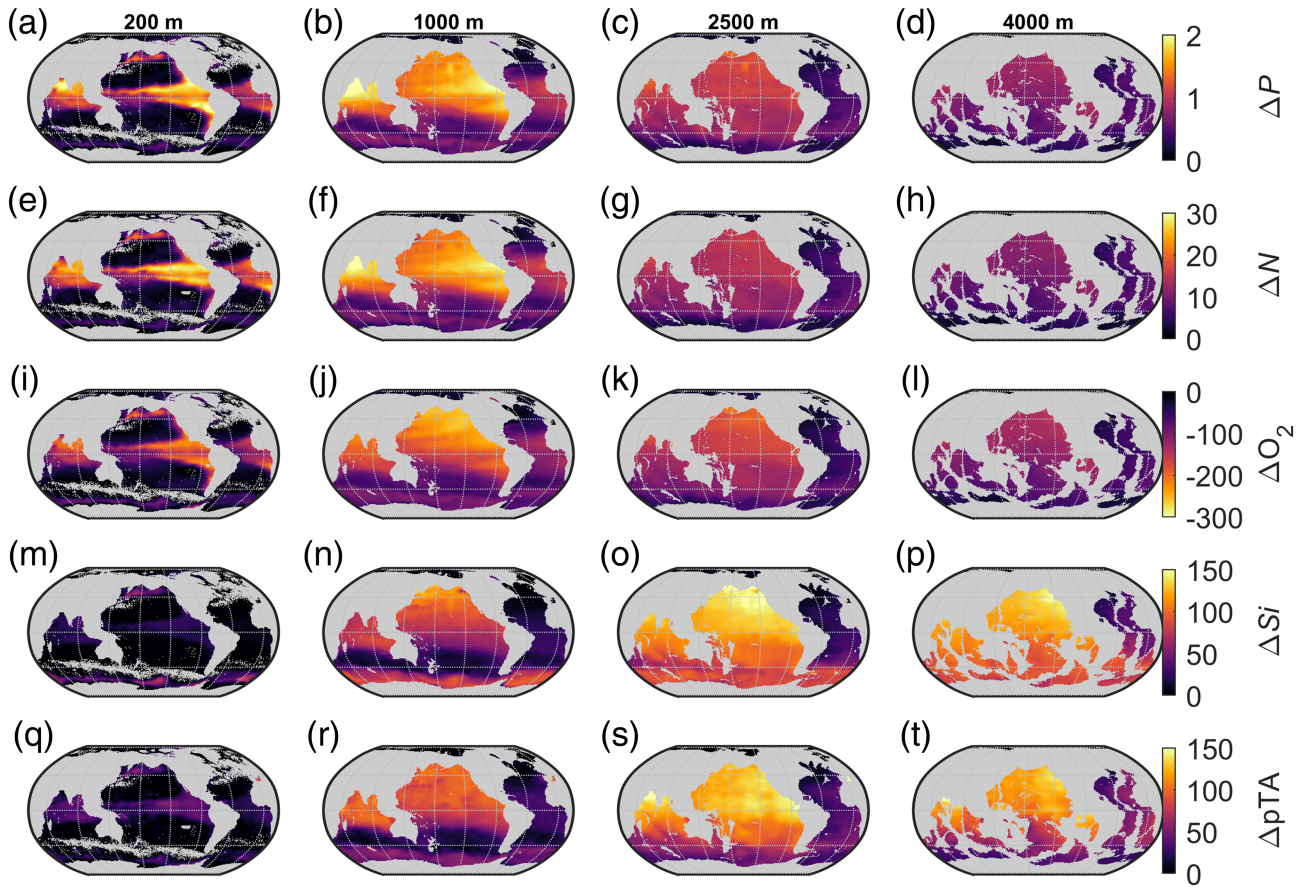

Figure 4. As in Figure 3 but showing accumulations, or the observed concentrations in excess of preformed concentrations.

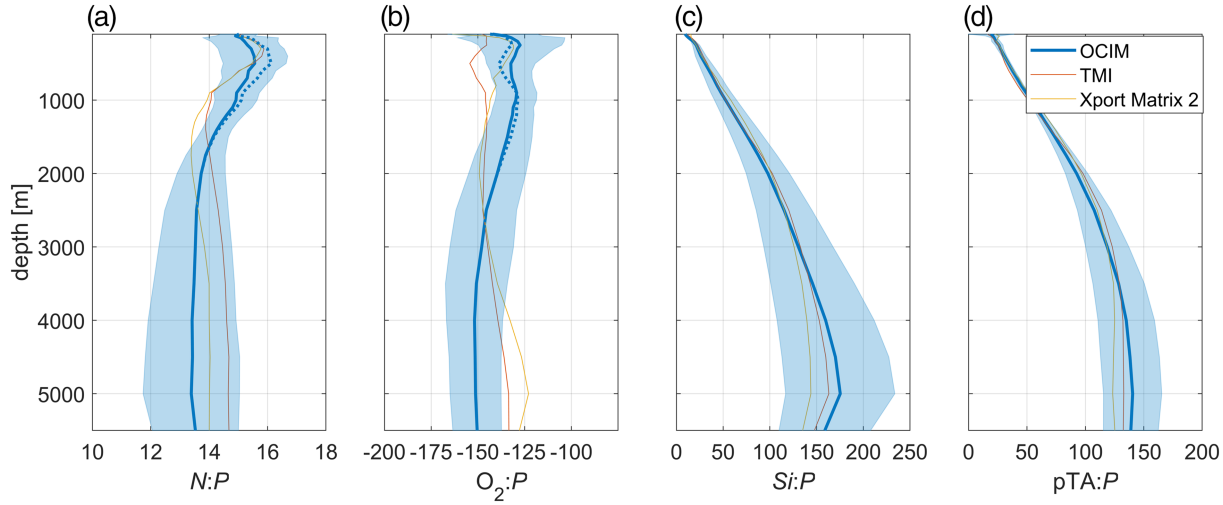

Figure 5. Mean relative accumulations (i.e., remineralization ratios) plotted against depth. The 0–100 m depth range is omitted from these calculations, along with regions with accumulations of phosphate less than 0.01 μmol kg^{-1} or oxygen accumulations less than 20 μmol kg^{-1}. The thick solid blue line reflects values returned using the OCIM circulation (with the blue patches reflecting ±1 standard uncertainties), while the thin orange and red lines are appropriate for Khatiwala (2007)'s transport matrix and the 2010 Total Matrix Intercomparison solution, respectively. The dotted blue lines in (a) and (b) are OCIM results omitting data from grid cells with <50 μmol kg^{-1} O_2 (i.e., limiting the influence of pelagic anerobic remineralization).

through the Indian and into the Pacific Ocean (Figure 4) reflecting continued remineralization of organic matter and dissolution of carbonate minerals as water flows along the deep ocean thermohaline circulation pathways, as well as the large volume of the Pacific Ocean (Table 1).

3.3. Remineralization Ratios

The remineralization ratios implied by the total quantities of property accumulations are (estimates ±1σ) [1 *P*]: [14.1 ± 0.6 *N*]: [−141 ± 12 O_2]: [95 ± 25 *Si*]: [89 ± 9 TA]. The average *Si*:P and pTA:P ratios increase with depth due to the deeper remineralization of $CaCO_3$ and biogenic *Si* relative to soft tissues (Figure 5).

Like Anderson and Sarmiento (1994) and DeVries et al. (2013), we find a N:P accumulation ratio that is below the traditional 16:1 "Redfield ratio," reflecting the impact of net denitrification in the subsurface ocean. Those earlier studies and ours also find that the N:P regeneration ratio reaches a minimum at depth (Figure 5a), although this minimum is extended shallower in the model of DeVries et al. (2013). Importantly, these earlier studies found regenerated N:P ratios of ~12:1 at their minimum, whereas we find a minimum N:P regeneration ratio of ~14:1. Our findings are similar whether using regression-based or interpolation-based estimates (Figure S4) and whether examining relative accumulations against depth (Figure 5) or regressing accumulations along isopycnal surfaces (not shown) as was done in both earlier studies. This finding appears to suggest smaller denitrification rates than are found by previous studies based on N deficits relative to expectations from P distributions (e.g., DeVries et al., 2013) but more likely reflects that the N:P ratio of fresh organic matter is >16:1 in low latitudes where denitrification is predominant.

The *N** tracer measures the difference between the observed N:P ratio and 16:1 to estimate the impacts of denitrification (Deutsch et al., 2001; Gruber & Sarmiento, 1997). As with other tracers, we can consider the difference between the observed and preformed N^* value, which represents the apparent accumulation of this tracer since water mass formation as Δ*N** (Figures 6a–6d):

$$N^*-N^{*0} = N - N^0 - 16\left(P - P^0\right) \equiv \Delta N^*. \quad (4)$$

The observation of positive ΔN^* at 200 m across the low-latitude Atlantic (Figure 6a; ±20°N) implies remineralization of organic matter with a >16:1 N:P ratio in this region specifically. High regional N:P ratios for organic matter remineralization are probably due in part to high rates of nitrogen fixation, particularly in the low-latitude Atlantic Ocean (Luo et al., 2014; Sohm et al., 2011; Wang et al., 2019). Variability in N:P ratios of organic matter remineralization could also reflect the N:P requirements of different

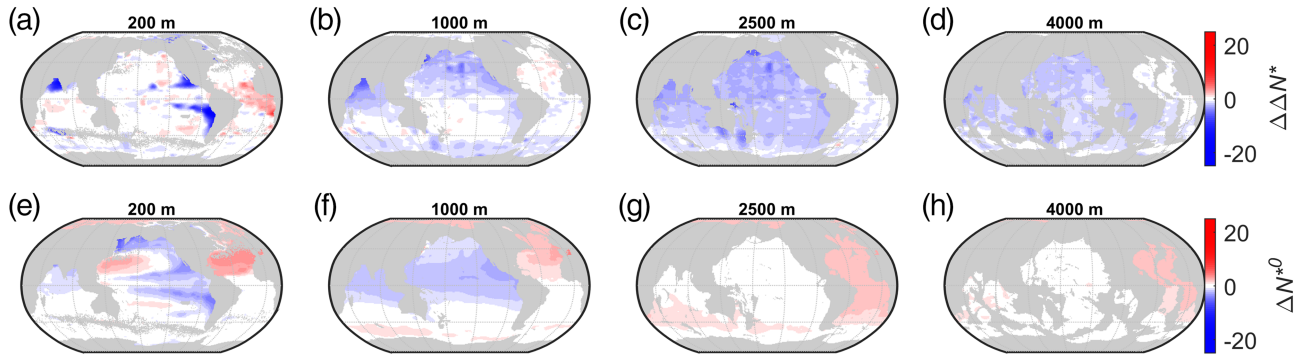

Figure 6. Maps on four depth surfaces of the change in the Δ*N** property relative to the preformed values. Blue areas indicate removal of N relative to P due to net denitrification or to remineralization of organic matter with a N:P ratio <16:1. Red areas indicate addition of N relative to P due to remineralization of organic matter with an N:P ratio >16:1, predominantly due to nitrogen fixation in surface waters that creates organic matter with elevated N:P.

phytoplankton assemblages, with large plankton such as diatoms that dominate the nutrient-rich high latitudes generally having lower N:P ratios (~10:1) than picoplankton that dominate the nutrient-poor low latitudes (~30:1) (Galbraith & Martiny, 2015; Klausmeler et al., 2004; Martiny et al., 2013; Weber & Deutsch, 2010). These variations are visible most clearly at 200 m depth, with the Southern Ocean having lower (negative or near-zero) Δ*N**, reflecting the remineralization of organic matter with low N:P, and the subtropics and low-latitude Atlantic having high Δ*N**, reflecting the remineralization of organic matter with high N:P either due to surface nitrogen fixation or preferential phosphate remineralization (Yoshikawa et al., 2013) at depths shallow enough to be included in our calculations as "preformed." Intensely negative Δ*N** in the Arabian Sea, the Eastern Tropical North Pacific, and the Peru (a.k.a. Humboldt), current reflects the influence of water-column denitrification (Figure 6a). At depths >200 m, the influence of stoichiometric variability is mostly obscured by the basin-scale patterns of nitrogen fixation and denitrification, with net denitrification in the Pacific and Indian Oceans imparting a negative Δ*N** signal in these basins (Figure 6).

The general trend toward more negative Δ*N** with depth (Figure 6) also reflects the influence of denitrification, primarily benthic denitrification in the deep ocean (Anderson & Sarmiento, 1994; DeVries et al., 2013). However, regional variations in export ratios of organic matter could imprint on the depth variability of Δ*N** and accumulation ratios (Figure 5a). Shallower waters preferentially accumulate the remineralization products of the low-latitude oceans where N:P ratios are highest, since the warmer subsurface waters are beneath the tropics and subtropics and induce shallow remineralization (DeVries & Weber, 2017; Weber et al., 2016). By contrast, the deep ocean accumulates the remineralization byproducts of lower N:P, higher *Si*:P high-latitude export that is remineralized deeper (Weber et al., 2016) and along isopycnals that connect the shallower portions of the high-latitude water columns with the deep ocean (Jenkins, 1987; Martin et al., 1987; Sonnerup et al., 2015). This provides an explanation for the net N:P ratio appearing highest over the ~200–700 m depth range dominated by the subtropical thermoclines where the impacts of water column denitrification—which is between a quarter and half of total denitrification—is near a maximum (Figure 5a). Variability in the N:P ratio of surface export implies additional constraints are required beyond Δ*N* and Δ*P* for a mass balance calculation of denitrification and nitrogen fixation impacts, though we suggest our data product could be used alongside independent information about nitrogen cycling, such as N_2/Ar measurements or isotopic constraints, for such a calculation in future work.

The N^{*0} (Figures 6e–6h), or preformed *N** shows how much of the *N** signal is inherited from the initial conditions of water masses, and thus how large errors would be for estimates that interpret *N**, rather than Δ*N**, as a signal accumulated since water mass formation. Broadly, it seems *N** would overestimate N deficits in the areas of strong denitrification in the eastern Pacific and the Subpolar North Pacific (north of 40°N), as well as the Indian Ocean to a lesser degree, while underestimating these deficits across the North Atlantic (north of 10°N, with this boundary moving southward with depth) and in the western portions of the subtropical North Pacific Gyre (between 10°N and 30°N and west of 150°W). This demonstrates the advantage of removing the preformed signal from the N^* field, as we have done with the ΔN^* tracer.

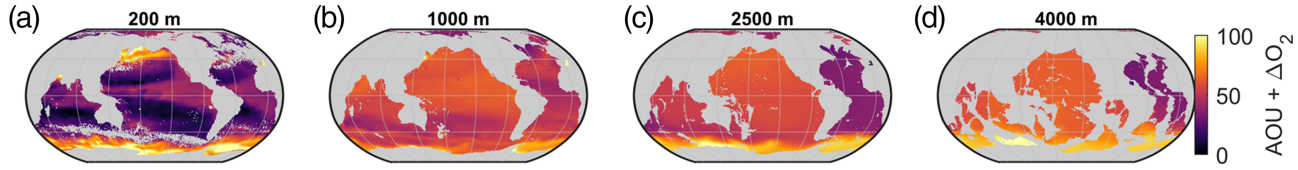

Figure 7. Maps of the excess in oxygen utilization suggested by AOU compared to estimates from the preformed O_2^0-based "accumulations" of this analysis for a range of depth surfaces. AOU is summed with ΔO_2 for these maps because ΔO_2 decreases and AOU increases when O_2 is consumed.

The -O_2:P ratio we determine (−141 ± 12) is significantly smaller than the ratios derived by Anderson and Sarmiento (1994) and Takahashi et al. (1985)'s analyses along isoneutral/isopycnal surfaces, but closer to the ratios found by early analyses (Redfield et al., 1963), and more recent studies using global nutrient distributions (DeVries & Deutsch, 2014) and observations of the biochemical composition of marine organic matter (Anderson, 1995; Emerson & Hedges, 2008). Early isopycnal analyses may have arrived at a too-high value for the -O_2:P ratio by neglecting dianeutral diffusion, as demonstrated by later studies (Carter, Talley, et al., 2014; Li & Peng, 2002).

3.4. Accumulated Oxygen Deficit Versus AOU

The accumulated oxygen deficit (i.e., ΔO_2) has a different interpretation and distribution than AOU. The latter considers O_2 consumption or loss since seawater was last fully equilibrated with respect to atmospheric oxygen, while the former considers the O_2 consumption since seawater last left contact with the surface mixed layer. The difference between these definitions (Figure 7) is significant for water masses in the Southern Ocean and in the western North Pacific. These water masses are dominated by mixtures between surface waters with interior ocean waters that have already experienced significant biological oxygen consumption (as discussed in section 3.1). It is known that AOU could be an overestimate for initial water mass oxygen saturation (Duteil et al., 2013; Ito et al., 2004). Our methodology suggests that AOU could overestimate oxygen consumption by amounts varying from 0 μmol kg^{-1} in subtropical gyre thermoclines to as much as 100 μmol kg^{-1} O_2 across the Southern Ocean (south of 60°S), and by ~30–100 μmol/kg in the deep ocean. These results support the model-based findings of Ito et al. (2004) and Duteil et al. (2012) and the observational-based estimates of Duteil et al. (2013). In summary, we find that 143 (±15) Pmol O_2 is consumed in the ocean following water mass formation, which is 73 Pmol (i.e., 34%) less than implied by AOU. This difference is similar to Duteil et al.'s (2013) estimate of a 25% overestimation with AOU inventories.

3.5. Sequestered Carbon and Carbonate Cycling

The overall property accumulations can be related to the strengths of the "hard" carbonate mineral and "soft" organic matter biological carbon pumps (we do not distinguish here between particulate and dissolved organic matter): Assuming a -O_2:*C* ratio of 1.4 (from, e.g., Anderson, 1995) for the soft tissue pump, our estimates imply a total of 1,230 (±140) PgC worth of C is stored through aerobic organic matter remineralization among the various interior ocean water masses. (PgC = GtC = 10^{15} g and only reflects the mass of the carbon atoms in carbon dioxide and carbonate ions and minerals.) These estimates are within uncertainties of the values obtained when scaling the 14.4 (±2.8) Pmol N accumulation with a C:N ratio of 6.6 to estimate a total storage of 1,150 (±220) PgC. Similarly, P accumulation with a C:P ratio of 106 implies a total storage of 1,300 (± 230) PgC. The -O_2:*C* ratio is more tightly constrained than the C:P ratio and might provide the best estimate. However, given that some nitrate is lost to denitrification, which oxidizes organic matter without consuming oxygen, it is not surprising that our estimate based on P is the largest of the three and that the nitrate based estimate is the smallest. The rain ratio of carbon stored as carbonate minerals relative to carbon stored as organic matter is thought to be small (e.g., 0.06 ± 0.03%; Sarmiento et al., 2002), yet potential TA accumulations suggest that the hard tissue pump stores 540 (±60) PgC, or ~40% of the soft tissue pump. This discrepancy is expected because carbonate mineral dissolution occurs deeper in the water column than organic matter remineralization on average (Figure 4d) and thus in water masses with longer residence times. As with other properties, the largest fraction of carbonate mineral dissolution byproducts is found in the Pacific, followed by the Indian and Atlantic Oceans (Table 1).

Berelson et al. (2007) use a similar approach for rate estimation to our age-regression approach described in Supporting Information S4 (i.e., regressing accumulations against ages), but with different age and alkalinity accumulation distributions. Our global carbonate mineral dissolution rate of 0.86 (±0.05) PgC yr^{-1} is smaller than the 1.4 PgC yr^{-1} found by Berelson et al. (2007) for the global ocean below 200 m depth but consistent with their literature-based range of surface ocean $CaCO_3$ export (0.4 to 1.8 PgC yr^{-1}). Our deep dissolution rate estimate of 0.49 (±0.04) PgC yr^{-1} below 1,500 m is slightly larger than their 0.4 PgC yr^{-1} estimate. Our estimate agrees closely with their 0.6 PgC yr^{-1} sediment trap-based estimate of $CaCO_3$ export across the 2,000 m depth surface, after subtracting their estimate of 0.1 PgC yr^{-1} burial in sediments. Our rate estimates are smaller for the 200 to 1,500 m depth range where we find 0.33 (±0.03) PgC yr^{-1} dissolution, and they find 1.0 PgC yr^{-1}. We therefore find deeper and less overall carbonate dissolution than Berelson et al. (2007). We attribute our slightly higher estimates for deep dissolution primarily to differences in the preformed property estimation strategy: the TA excesses given by the method used by Berelson et al. (2007)—as articulated by Feely et al. (2002)—average 0 to 65 μmol kg^{-1} TA less across the Pacific Ocean than our ΔpTA estimates, with the differences peaking near 3,000 m depth and being more than 50 μmol kg^{-1} at all depths below 1,500 m. The lower shallow-depth estimates we attribute to differences in our age estimation strategy: The CFC-11 dating technique used by Berelson et al. (2007) for this depth range can be biased by mixing toward younger age estimates in older waters (Mecking, 2004; Sonnerup, 2001) and also cannot return age estimates that are older than the beginning of the period of strong atmospheric CFC-11 growth in the ~1960s (e.g., Sonnerup et al., 2015). Thus, the CFC-11 ages for the 26.65 kg m^{-3} σ_θ potential density anomaly surface were never greater than 30 yr for the 1990's WOCE data used by Feely et al. (2002). By contrast, our age estimates for the 26.6 to 26.7 kg m^{-3} σ_θ density anomaly average 130 (±80 standard deviation) yr, so our potential alkalinity excesses are estimated to accumulate over a much longer time interval. Like Berelson et al.'s (2007) estimates, our accumulation estimates reflect net dissolution and therefore do not include benthic calcification—which may be significant (e.g., Lebrato et al., 2010)—except as a net loss when precipitated benthic carbonate minerals are buried.

Some scientific discussion has focused on whether open ocean carbonate mineral dissolution is dominated by thermodynamically favored dissolution in undersaturated depths and regions of the ocean or whether dissolution in supersaturated regions (possibly in undersaturated microenvironments such as zooplankton guts) represents a meaningful fraction of the overall dissolution (e.g., Berelson et al., 2007; Feely et al., 2002; Milliman et al., 1999; Schiebel, 2002). We find that only 4% (±1%) of the byproducts of dissolution that accumulated since water mass formation reside within portions of the ocean that are supersaturated with respect to aragonite ($\Omega_A > 1$) while almost half (46% ± 5%) are found in calcite-supersaturated seawater ($\Omega_C > 1$). Dissolution rate estimates for these three saturation regimes ($\Omega_A > 1$, $\Omega_C > 1$, and $\Omega_C < 1$) indicate faster dissolution in supersaturated waters, but the differences are only barely significant given the uncertainties (which are potentially underestimated; see Supporting Information S4): the net rates are 0.12 (±0.02), 0.12 (±0.01), and 0.09 (±0.01) μmol pTA kg^{-1} yr^{-1} for $\Omega_A > 1$, $\Omega_C > 1$, and $\Omega_C < 1$, respectively. It is clear that large differences in overall accumulation are primarily a consequence of differences in the volumes and the mean ages of the reservoirs with the much larger deeper accumulation reflecting a much larger water volume and older age. These values do not include dissolution occurring within mixed layers or in portions of the water column shallower than 100 m and therefore may be underestimated, particularly for the aragonite saturation-specific estimate because the aragonite saturation horizon is near 100 m through much of the North Pacific. Overall, this discussion suggests that although carbonate mineral dissolution in supersaturated environments may have been previously overestimated (Carter, Talley, et al., 2014; Friis et al., 2006, 2007), there are nevertheless carbonate mineral dissolution byproducts found (and likely accumulating) above the aragonite saturation horizon.

4. Conclusions

We presented preformed property distributions estimated using recent circulation and ventilation pathway reconstructions with several recently developed (and three new) empirical property estimation algorithms. We showed how global ocean preformed property distributions arise as combinations of four broad classes of interior ocean water masses (NADW, AABW, intermediate and mode waters, and shallow subtropical thermocline waters).

We explored variability in observed macronutrient and oxygen distributions, estimating net regeneration ratios of [1 *P*]: [14.1 ± 0.6 *N*]: [−141 ± 12 O_2]: [95 ± 25 *Si*]: [89 ± 9 TA]. We provided evidence that organic matter N:P remineralization ratios greater than 16:1 occur in the Atlantic Ocean. In light of recent findings of regional N:P ratio variability, we also argue that high-latitude export of silicate and phosphate-rich organic matter could be an additional control for variability of apparent macronutrient accumulation ratios with depth (beyond a well-studied impact from denitrification). Our N budget is underconstrained when allowing for flexible N:P of surface export, so we suggest further research combining independent denitrification constraints with our preformed macronutrient distributions could be used to close the budget for nitrogen cycling. We found that AOU overestimates oxygen utilization since water mass formation by ~34%, confirming previous analyses that showed that AOU overestimates oxygen consumption due to O_2 undersaturation during water mass subduction and oxygen loss due to mixing and organic matter remineralization.

We estimated accumulation rates of $CaCO_3$ and confirmed the results of earlier studies, suggesting that, although there is a significant accumulated alkalinity from dissolution of $CaCO_3$ above both the aragonite and calcite saturation horizons, this dissolution may have been overestimated by previous studies: We find that only 4% (±1%) and 46% (±5%) of the byproducts of carbonate mineral dissolution are found above the aragonite and calcite saturation horizons, respectively. Our best estimates of regional dissolution rates imply that the dissolution rate is fairly uniform across depths, but we caution (in section 2.4 and Supporting Information S4) that considerable—and poorly quantified—uncertainties remain for these alkalinity-excess-based rate estimates due to potential methodological biases. Our analysis suggests that the ocean sequesters ~540 (±60) PgC worth of carbon as dissolved carbonate minerals, compared to the 1,230 (±230) PgC as organic matter respired by bacteria and animals implied by oxygen deficits. Calculations based on AOU rather than O_2 would overestimate organic matter respiration in the interior ocean by ~33%, due to O_2 consumption that occurs prior to water mass formation.

While our preformed property estimates are improvements over earlier estimates, there remain considerable uncertainties (that are separately estimated in the supporting information and presented alongside the preformed property estimates). We anticipate that further development of property estimation algorithms and interior ocean mixing pathway reconstructions could improve the preformed property fields. In particular, the large quantities of data being produced by the nascent biogeochemical Argo array (e.g., Johnson & Claustre, 2016) will alleviate the large seasonal biases in our observations of biogeochemical properties, which will help to generate better-constrained data assimilated model products and empirical regression property estimation algorithms.

Data Availability Statement

The preformed property estimates are archived via Zenodo (under https://doi.org/10.5281/zenodo.3745002). External data sets for this research are published by Holte et al. (2017), Lauvset et al. (2016), and Olsen et al. (2016).

Acknowledgments
We thank the Ocean Observations and Monitoring Division of the National Oceanic and Atmospheric Administration for funding this research (Project 100007298), which was used to develop these data products and related methods. This is PMEL Contribution Number 5084 and JISAO Contribution Number 2020-1058.

References

Anderson, L. A. (1995). On the hydrogen and oxygen content of marine phytoplankton. *Deep Sea Research Part I: Oceanographic Research Papers*, *42*(9), 1675–1680. https://doi.org/10.1016/0967-0637(95)00072-E

Anderson, L. A., & Sarmiento, J. L. (1994). Redfield ratios of remineralization determined by nutrient data analysis. *Global Biogeochemical Cycles*, *8*(1), 65–80. https://doi.org/10.1029/93GB03318

Berelson, W. M., Balch, W. M., Najjar, R., Feely, R. A., Sabine, C., & Lee, K. (2007). Relating estimates of $CaCO_3$ production, export, and dissolution in the water column to measurements of $CaCO_3$ rain into sediment traps and dissolution on the sea floor: A revised global carbonate budget. *Global Biogeochemical Cycles*, *21*, GB1024. https://doi.org/10.1029/2006GB002803

Broecker, W. S. (1974). "NO," a conservative water-mass tracer. *Earth and Planetary Science Letters*, *23*(1), 100–107. https://doi.org/10.1016/0012-821X(74)90036-3

Carter, B. R., Feely, R. A., Williams, N. L., Dickson, A. G., Fong, M. B., & Takeshita, Y. (2017). Updated methods for global locally interpolated estimation of alkalinity, pH, and nitrate. *Limnology and Oceanography: Methods*, *16*(2), 119–131. https://doi.org/10.1002/lom3.10232

Carter, B. R., Talley, L. D., & Dickson, A. G. (2014). Mixing and remineralization in waters detrained from the surface into Subantarctic Mode Water and Antarctic Intermediate Water in the southeastern Pacific. *Journal of Geophysical Research: Oceans*, *119*, 4001–4028. https://doi.org/10.1002/2013JC009355

Carter, B. R., Toggweiler, J. R., Key, R. M. M., & Sarmiento, J. L. L. (2014). Processes determining the marine alkalinity and calcium carbonate saturation state distributions. *Biogeosciences*, *11*(24), 7349–7362. https://doi.org/10.5194/bg-11-7349-2014

Carter, B. R., Williams, N. L., Gray, A. R., & Feely, R. A. (2016). Locally interpolated alkalinity regression for global alkalinity estimation. *Limnology and Oceanography: Methods*, *14*(4), 268–277. https://doi.org/10.1002/lom3.10087

Deutsch, C., Gruber, N., Key, R. M., Sarmiento, J. L., & Ganachaud, A. (2001). Denitrification and N_2 fixation in the Pacific Ocean. *Global Biogeochemical Cycles*, *15*(2), 483–506. https://doi.org/10.1029/2000GB001291

Deutsch, C., & Weber, T. (2012). Nutrient ratios as a tracer and driver of ocean biogeochemistry. *Annual Review of Marine Science*, *4*(1), 113–141. https://doi.org/10.1146/annurev-marine-120709-142821

Devries, T. (2014). The oceanic anthropogenic CO_2 sink: Storage, air-sea fluxes, and transports over the industrial era. *Global Biogeochemical Cycles*, *28*, 631–647. https://doi.org/10.1002/2013GB004739

DeVries, T., & Deutsch, C. (2014). Large-scale variations in the stoichiometry of marine organic matter respiration. *Nature Geoscience*, *7*(12), 890–894. https://doi.org/10.1038/ngeo2300

DeVries, T., Deutsch, C., Rafter, P. A., & Primeau, F. (2013). Marine denitrification rates determined from a global 3-D inverse model. *Biogeosciences*, *10*(4), 2481–2496. https://doi.org/10.5194/bg-10-2481-2013

DeVries, T., & Weber, T. (2017). The export and fate of organic matter in the ocean: New constraints from combining satellite and oceanographic tracer observations. *Global Biogeochemical Cycles*, *31*, 535–555. https://doi.org/10.1002/2016GB005551

DeVries, T., & Primeau, F. (2011). Dynamically and observationally constrained estimates of water-mass distributions and ages in the Global Ocean. *Journal of Physical Oceanography*, *41*(12), 2381–2401. https://doi.org/10.1175/JPO-D-10-05011.1

Dunne, J. P., Sarmiento, J. L., & Gnanadesikan, A. (2007). A synthesis of global particle export from the surface ocean and cycling through the ocean interior and on the seafloor. *Global Biogeochemical Cycles*, *21*, GB4006. https://doi.org/10.1029/2006GB002907

Duteil, O., Koeve, W., Oschlies, A., Aumont, O., Bianchi, D., Bopp, L., et al. (2012). Preformed and regenerated phosphate in ocean general circulation models: Can right total concentrations be wrong? *Biogeosciences*, *9*(5), 1797–1807. https://doi.org/10.5194/bg-9-1797-2012

Duteil, O., Koeve, W., Oschlies, A., Bianchi, D., Galbraith, E., Kriest, I., & Matear, R. (2013). A novel estimate of ocean oxygen utilisation points to a reduced rate of respiration in the ocean interior. *Biogeosciences*, *10*(11), 7723–7738. https://doi.org/10.5194/bg-10-7723-2013

Emerson, S., & Hedges, J. (2008). Chemical oceanography and the marine carbon cycle. Retrieved from https://books.google.com/books?hl=en&lr=&id=BwRSn2ikJW4C&oi=fnd&pg=PR9&dq=emerson+and+hedges+chemical+oceanography&ots=xFGy4iNsgb&sig=rbyL-nz4OE0nvzbVhPecxt-EKrc

Feely, R. A., Alin, S. R., Carter, B. R., Bednaršek, N., Hales, B., Chan, F., et al. (2016). Chemical and biological impacts of ocean acidification along the west coast of North America. *Estuarine, Coastal and Shelf Science*, *183*, 260–270. https://doi.org/10.1016/j.ecss.2016.08.043

Feely, R. A., Sabine, C. L., Lee, K., Berelson, W., Kleypas, J., Fabry, V. J., & Millero, F. J. (2004). Impact of anthropogenic CO_2 on the $CaCO_3$ system in the oceans. *Science (New York, N.Y.)*, *305*(5682), 362–366. https://doi.org/10.1126/science.1097329

Feely, R. A., Sabine, C. L., Lee, K., Millero, F. J., Lamb, M. F., Greeley, D., et al. (2002). In situ calcium carbonate dissolution in the Pacific Ocean. *Global Biogeochemical Cycles*, *16*(4), 1144. https://doi.org/10.1029/2002GB001866

Feely, R. A., Sabine, C. L., Schlitzer, R., Bullister, J. L., Mecking, S., & Greeley, D. (2004). Oxygen utilization and organic carbon remineralization in the upper water column of the Pacific Ocean. *Journal of Oceanography*, *60*(1), 45–52. https://doi.org/10.1023/B:JOCE.0000038317.01279.aa

Francois, R., Honjo, S., Krishfield, R., & Manganini, S. (2002). Factors controlling the flux of organic carbon to the bathypelagic zone of the ocean. *Global Biogeochemical Cycles*, *16*(4), 1087. https://doi.org/10.1029/2001GB001722

Friis, K., Najjar, R. G., Follows, M. J., & Dutkiewicz, S. (2006). Possible overestimation of shallow-depth calcium carbonate dissolution in the ocean. *Global Biogeochemical Cycles*, *20*, GB4019. https://doi.org/10.1029/2006GB002727

Friis, K., Najjar, R. G., Follows, M. J., Dutkiewicz, S., Körtzinger, A., & Johnson, K. M. (2007). Dissolution of calcium carbonate: Observations and model results in the subpolar North Atlantic. *Biogeosciences*, *4*(2), 205–213. Retrieved from. www.biogeosciences.net/4/205/2007/, https://doi.org/10.5194/bg-4-205-2007

Galbraith, E. D., & Martiny, A. C. (2015). A simple nutrient-dependence mechanism for predicting the stoichiometry of marine ecosystems. *Proceedings of the National Academy of Sciences*, *112*(27), 8199–8204. https://doi.org/10.1073/pnas.1423917112

Gebbie, G., Huybers, P., Gebbie, G., & Huybers, P. (2010). Total matrix intercomparison: A method for determining the geometry of water-mass pathways. *Journal of Physical Oceanography*, *40*(8), 1710–1728. https://doi.org/10.1175/2010JPO4272.1

Gruber, N., & Sarmiento, J. L. (1997). Global patterns of marine nitrogen fixation and denitrification. *Global Biogeochemical Cycles*, *11*(2), 235–266. https://doi.org/10.1029/97GB00077

Hedges, J. I., Baldock, J. A., Gélinas, Y., Lee, C., Peterson, M. L., & Wakeham, S. G. (2002). The biochemical and elemental compositions of marine plankton: A NMR perspective. *Marine Chemistry*, *78*(1), 47–63. https://doi.org/10.1016/S0304-4203(02)00009-9

Henson, S. A., Sanders, R., & Madsen, E. (2012). Global patterns in efficiency of particulate organic carbon export and transfer to the deep ocean. *Global Biogeochemical Cycles*, *26*, GB1028. https://doi.org/10.1029/2011GB004099

Holte, J., Talley, L. D., Gilson, J., & Roemmich, D. (2017). An Argo mixed layer climatology and database. *Geophysical Research Letters*, *44*, 5618–5626. https://doi.org/10.1002/2017GL073426

Holzer, M., Primeau, F. W., DeVries, T., & Matear, R. (2014). The Southern Ocean silicon trap: Data-constrained estimates of regenerated silicic acid, trapping efficiencies, and global transport paths. *Journal of Geophysical Research: Oceans*, *119*, 313–331. https://doi.org/10.1002/2013JC009356

Honjo, S., Manganini, S. J., Krishfield, R. A., & Francois, R. (2008). Particulate organic carbon fluxes to the ocean interior and factors controlling the biological pump: A synthesis of global sediment trap programs since 1983. *Progress in Oceanography*, *76*(3), 217–285. https://doi.org/10.1016/J.POCEAN.2007.11.003

Ingle, S. E. (1975). Solubility of calcite in the ocean. *Marine Chemistry*, *3*(4), 301–319. https://doi.org/10.1016/0304-4203(75)90010-9

Ito, T., Follows, M. J., & Boyle, E. A. (2004). Is AOU a good measure of respiration in the oceans? *Geophysical Research Letters*, *31*, L17305. https://doi.org/10.1029/2004GL020900

Jenkins, W. (1987). ^{3}H and ^{3}He in the beta triangle: Observations of gyre ventilation and oxygen utilization rates. *Journal of Physical Oceanography*, *17*(6), 763–783. https://doi.org/10.1175/1520-0485(1987)017<0763:AITBTO>2.0.CO;2

Jiang, L.-Q., Feely, R. A., Carter, B. R., Greeley, D. J., Gledhill, D. K., & Arzayus, K. M. (2015). Climatological distribution of aragonite saturation state in the global oceans. *Global Biogeochemical Cycles*, *29*, 1656–1673. https://doi.org/10.1002/2015GB005198

Johnson, K., & Claustre, H. (2016). Bringing biogeochemistry into the Argo age. *EOS. Transactions of the American Geophysical Union*, *97*. https://doi.org/10.1029/2016EO062427

Khatiwala, S. (2007). A computational framework for simulation of biogeochemical tracers in the ocean. *Global Biogeochemical Cycles*, *21*, GB3001. https://doi.org/10.1029/2007GB002923

Klaas, C., & Archer, D. E. (2002). Association of sinking organic matter with various types of mineral ballast in the deep sea: Implications for the rain ratio. *Global Biogeochemical Cycles*, *16*(4), 1116. https://doi.org/10.1029/2001GB001765

Klausmeler, C. A., Litchman, E., Daufreshna, T., & Levin, S. A. (2004). Optimal nitrogen-to-phosphorus stoichiometry of phytoplankton. *Nature*, *429*(6988), 171–174. https://doi.org/10.1038/nature02454

Koeve, W., & Kähler, P. (2016). Oxygen utilization rate (OUR) underestimates ocean respiration: A model study. *Global Biogeochemical Cycles*, *30*, 1166–1182. https://doi.org/10.1002/2015GB005354

Lauvset, S. K., Carter, B. R., Perez, F. F., Jiang, L.-Q., Feely, R. A., Velo, A., & Olsen, A. (2020). Processes driving global interior ocean pH distribution. *Global Biogeochemical Cycles*, *34*, e2019GB006229. https://doi.org/10.1029/2019GB006229

Lauvset, S. K., Key, R. M., Olsen, A., van Heuven, S., Velo, A., Lin, X., et al. (2016). A new global interior ocean mapped climatology: The 1° × 1° GLODAP version 2. *Earth System Science Data*, *8*(2), 325–340. https://doi.org/10.5194/ESSD-8-325-2016

Lebrato, M., Iglesias-Rodríguez, D., Feely, R. A., Greeley, D., Jones, D. O. B., Suarez-Bosche, N., et al. (2010). Global contribution of echinoderms to the marine carbon cycle: $CaCO_3$ budget and benthic compartments. *Ecological Monographs*, *80*(3), 441–467. https://doi.org/10.1890/09-0553.1

Li, Y.-H., & Peng, T.-H. (2002). Latitudinal change of remineralization ratios in the oceans and its implication for nutrient cycles. *Global Biogeochemical Cycles*, *16*(4), 1130. https://doi.org/10.1029/2001GB001828

Luo, Y.-W., Lima, I. D., Karl, D. M., Deutsch, C. A., & Doney, S. C. (2014). Data-based assessment of environmental controls on global marine nitrogen fixation. *Biogeosciences*, *11*(3), 691–708. https://doi.org/10.5194/bg-11-691-2014

Marinov, I., Gnanadesikan, A., Sarmiento, J. L., Toggweiler, J. R., Follows, M., & Mignone, B. K. (2008). Impact of oceanic circulation on biological carbon storage in the ocean and atmospheric pCO_2. *Global Biogeochemical Cycles*, *22*, GB3007. https://doi.org/10.1029/2007GB002958

Martin, J. H., Knauer, G. A., Karl, D. M., & Broenkow, W. W. (1987). VERTEX: Carbon cycling in the northeast Pacific. *Deep Sea Research Part A. Oceanographic Research Papers*, *34*(2), 267–285. https://doi.org/10.1016/0198-0149(87)90086-0

Martiny, A. C., Pham, C. T. A., Primeau, F. W., Vrugt, J. A., Moore, J. K., Levin, S. A., & Lomas, M. W. (2013). Strong latitudinal patterns in the elemental ratios of marine plankton and organic matter. *Nature Geoscience*, *6*(4), 279–283. https://doi.org/10.1038/ngeo1757

Mecking, S. (2004). Influence of mixing on CFC uptake and CFC ages in the North Pacific thermocline. *Journal of Geophysical Research*, *109*, C07014. https://doi.org/10.1029/2003JC001988

Milliman, J. D., & Droxler, A. W. (1996). Neritic and pelagic carbonate sedimentation in the marine environment: Ignorance is not bliss. *Geologische Rundschau*, *85*(3), 496–504. https://doi.org/10.1007/BF02369004

Milliman, J. D., Troy, P. J., Balch, W. M., Adams, A. K., Li, Y.-H., & Mackenzie, F. T. (1999). Biologically mediated dissolution of calcium carbonate above the chemical lysocline? *Deep Sea Research Part I: Oceanographic Research Papers*, *46*(10), 1653–1669. https://doi.org/10.1016/S0967-0637(99)00034-5

Naveira Garabato, A. C., Jullion, L., Stevens, D. P., Heywood, K. J., & King, B. A. (2009). Variability of Subantarctic Mode Water and Antarctic Intermediate Water in the Drake Passage during the late-twentieth and early-twenty-first centuries. *Journal of Climate*, *22*(13), 3661–3688. https://doi.org/10.1175/2009JCLI2621.1

Olsen, A., Key, R. M., van Heuven, S., Lauvset, S. K., Velo, A., Lin, X., et al. (2016). The Global Ocean Data Analysis Project Version 2 (GLODAPv2) – An internally consistent data product for the world ocean. *Earth System Science Data*, *8*(2), 297–323. https://doi.org/10.5194/essd-8-297-2016

Pardo, P. C., Vázquez-Rodríguez, M., Pérez, F. F., & Rios, A. F. (2011). CO_2 air-sea disequilibrium and preformed alkalinity in the Pacific and Indian oceans calculated from subsurface layer data. *Journal of Marine Systems*, *84*(3–4), 67–77. https://doi.org/10.1016/J.JMARSYS.2010.08.006

Redfield, A. C. (1934). On the proportions of organic derivatives in sea water and their relation to the composition of plankton. *James Johnstone Memorial Volume*, 176–192. Retrieved from. https://ci.nii.ac.jp/naid/10006798977/

Redfield, A. C., Ketchum, B. H., & Richards, A. F. (1963). The influence of organisms on the composition of seawater. *The Sea*, *2*, 26–77.

Russell, J. L., & Dickson, A. G. (2003). Variability in oxygen and nutrients in South Pacific Antarctic Intermediate Water. *Global Biogeochemical Cycles*, *17*(2), 1033. https://doi.org/10.1029/2000GB001317

Sabine, C. L., Feely, R. A., Gruber, N., Key, R. M., Lee, K., Bullister, J. L., et al. (2004). The oceanic sink for anthropogenic CO_2. *Science (New York, N.Y.)*, *305*(5682), 367–371. https://doi.org/10.1126/science.1097403

Sabine, C. L., Feely, R. A., Key, R. M., Bullister, J. L., Millero, F. J., Lee, K., et al. (2002). Distribution of anthropogenic CO_2 in the Pacific Ocean. *Global Biogeochemical Cycles*, *16*(4), 1083. https://doi.org/10.1029/2001GB001639

Sabine, C. L., & Tanhua, T. (2010). Estimation of anthropogenic CO_2 inventories in the ocean. *Annual Review of Marine Science*, *2*(1), 175–198. https://doi.org/10.1146/annurev-marine-120308-080947

Sarmiento, J. L., Dunne, J., Gnanadesikan, A., Key, R. M., Matsumoto, K., & Slater, R. (2002). A new estimate of the $CaCO_3$ to organic carbon export ratio. *Global Biogeochemical Cycles*, *16*(4), 1107. https://doi.org/10.1029/2002GB001919

Sarmiento, J. L., Gruber, N., Brzezinski, M. A., & Dunne, J. P. (2004). High-latitude controls of thermocline nutrients and low latitude biological productivity. *Nature*, *427*(6969), 56–60. https://doi.org/10.1038/nature02127

Schiebel, R. (2002). Planktic foraminiferal sedimentation and the marine calcite budget. *Global Biogeochemical Cycles*, *16*(4), 1065. https://doi.org/10.1029/2001GB001459

Sohm, J. A., Webb, E. A., & Capone, D. G. (2011). Emerging patterns of marine nitrogen fixation. *Nature Reviews Microbiology*, *9*(7), 499–508. https://doi.org/10.1038/nrmicro2594

Sonnerup, R. E. (2001). On the relations among CFC derived water mass ages. *Geophysical Research Letters*, *28*(9), 1739–1742. https://doi.org/10.1029/2000GL012569

Sonnerup, R. E., Mecking, S., Bullister, J. L., & Warner, M. J. (2015). Transit time distributions and oxygen utilization rates from chlorofluorocarbons and sulfur hexafluoride in the Southeast Pacific Ocean. *Journal of Geophysical Research: Oceans*, *120*, 3761–3776. https://doi.org/10.1002/2015JC010781

Stommel, H. (1979). Determination of water mass properties of water pumped down from the Ekman layer to the geostrophic flow below. *Proceedings of the National Academy of Sciences*, *76*(7), 3051–3055. https://doi.org/10.1073/pnas.76.7.3051

Takahashi, T., Broecker, W. S., & Langer, S. (1985). Redfield ratio based on chemical data from isopycnal surfaces. *Journal of Geophysical Research*, *90*(C4), 6907. https://doi.org/10.1029/JC090iC04p06907

Talley, L. D. (2013). Closure of the global overturning circulation through the Indian, Pacific, and Southern Oceans: Schematics and transports. *Oceanography. Oceanography Society*. https://doi.org/10.2307/24862019

Talley, L. D., Lobanov, V., Ponomarev, V., Salyuk, A., Tishchenko, P., Zhabin, I., & Riser, S. (2003). Deep convection and brine rejection in the Japan Sea. *Geophysical Research Letters*, *30*(4), 1159. https://doi.org/10.1029/2002GL016451

Teng, Y., Primeau, F. W., Moore, J. K., Lomas, M. W., & Martiny, A. C. (2014). Global-scale variations of the ratios of carbon to phosphorus in exported marine organic matter. *Nature Geoscience*, *7*(12), 895–898. https://doi.org/10.1038/ngeo2303

Wang, W. L., Moore, J. K., Martiny, A. C., & Primeau, F. W. (2019). Convergent estimates of marine nitrogen fixation. *Nature*, *566*(7743), 205–211. https://doi.org/10.1038/s41586-019-0911-2

Weber, T., Cram, J. A., Leung, S. W., DeVries, T., & Deutsch, C. (2016). Deep ocean nutrients imply large latitudinal variation in particle transfer efficiency. *Proceedings of the National Academy of Sciences of the United States of America*, *113*(31), 8606–8611. https://doi.org/10.1073/pnas.1604414113

Weber, T. S., & Deutsch, C. (2010). Ocean nutrient ratios governed by plankton biogeography. *Nature*, *467*(7315), 550–554. https://doi.org/10.1038/nature09403

Wolf-Gladrow, D. A., Zeebe, R. E., Klaas, C., Körtzinger, A., & Dickson, A. G. (2007). Total alkalinity: The explicit conservative expression and its application to biogeochemical processes. *Marine Chemistry*, *106*(1–2), 287–300. https://doi.org/10.1016/j.marchem.2007.01.006

Yoshikawa, C., Coles, V. J., Hood, R. R., Capone, D. G., & Yoshida, N. (2013). Modeling how surface nitrogen fixation influences subsurface nutrient patterns in the North Atlantic. *Journal of Geophysical Research: Oceans*, *118*, 2520–2534. https://doi.org/10.1002/jgrc.20165